

Study on the evolution of dynamic characteristics and seismic damage of a self-centering concrete structure based on data-driven methods

Tianyang Zhang^a, Weizhi Xu^{a,*}, Shuguang Wang^{a,*}, Dongsheng Du^a, Qisong Miao^b

^a College of Civil Engineering, Nanjing Tech University, Nanjing, China

^b Beijing Institute of Architectural Design, Beijing, China

ARTICLE INFO

Keywords:

Earthquake damage
Unbonded post-tensioned prestress
Self-centering frame structure
Incremental dynamic analysis
Data-driven

ABSTRACT

This study concerns on the dynamic characteristics and seismic damage evaluation of a representative precast self-centering concrete frame (PSCCF) structure. A numerical model of the PSCCF was established using OpenSees software, and incremental dynamic analyses (IDA) were carried out. The structural frequency was obtained from displacement time-history responses using a synchrosqueezing continuous wavelet transform (SSQCWT), and the time-frequency distributions were statistically analysed. During seismic excitations, both the medium structural frequency and the post-seismic frequency of the PSCCF decrease with an increase in peak ground acceleration (PGA). The results demonstrated that the PSCCF suffered irreversible damage under significant deformation, also confirmed by the relatively large elongation rates of the post-tensioned (PT) strands and unbonded energy-dissipating bars (EDBs). Furthermore, this research uses convolutional neural networks (CNN) to predict the damage state of PSCCF, and employs gradient-weighted class activation mapping (Grad-CAM) and Gradient-Shap techniques to interpret the convolutional layers. The interpreted results show that the algorithm tends to use lower-frequency signal components to predict the structural damage state, and the data-driven results are consistent with human experience.

1. Introduction

Self-centering structures, which serve as solutions for functionally recoverable seismic structures, are currently a pivotal area of academic research [1–4]. In contrast to traditional cast-in-place reinforced concrete (RC) structures, which dissipate seismic energy through self-cracking and deformation [5–7], self-centering structures exhibit minimal post-earthquake residual deformation and damage, enabling swift restoration of the functionality of structures [8–10]. In the 1990s, the United States and Japan jointly conducted a decade-long precast structural seismic systems (PRESSS) program and proposed a pre-fabricated concrete frame structure system that used post-tensioned hybrid connections with the ability to autonomously self-center after earthquakes. Based on a substantial number of hybrid connection experiments [11–14], Priestley et al. [15–17] designed a five-story precast prestressed concrete structure and conducted low-cycle reciprocating tests, demonstrating that self-centering structures possess significant seismic resistance and reliability. Relying on the hybrid connections proposed in the PRESSS, self-centering frame structures have been constructed in regions such as the United States [18] and New Zealand

[19], and have withstood tests of actual earthquakes.

Inspired by the PRESSS program, many scholars worldwide have worked toward developing self-centering connections. Ozden et al. [20] explored the ratio of unbonded energy-dissipating bars with hybrid connections to the bearing capacity of beam ends, and the results showed that a ratio of 20%–30% could create connections with lower residual deformation and better energy-dissipating capacity. Pan et al. [21–23] conducted a series of investigations on the hysteresis properties of hybrid connections with and without plates. The low-cycle reciprocating tests showed that smoothing the contact surface between the beams, columns, and plates can reduce plate damage in hybrid connections. Wang et al. [24,25] explored the unbonded length and materials of energy-dissipating bars in hybrid connections and investigated repair methods for damaged connections. The results indicated that the seismic resistance of the hybrid connections could be restored through repairs. Lu et al. [26–28] conducted shaking table tests on unbonded prestressed post-tensioned self-centering frames, and the results showed that the structures exhibited good seismic performance. Although the inter-storey drift of the structure reached 2.45% during the excitation process, the residual deformation after the earthquake could be ignored,

* Corresponding authors.

E-mail addresses: xuwz@njtech.edu.cn (W. Xu), 720108@vip.sina.com (S. Wang).

and the application and promotion of self-centering structures in seismic regions were feasible. Zhou et al. [29–32] conducted low-cycle reciprocating tests on 29 hybrid connections with different characteristics and proposed a damage calculation model for these connections. The results showed that the initial prestress did not affect the damage states of the hybrid connections. However, increasing the stirrup ratio and concrete strength could reduce the damage under large deformations. Mao et al. [33] designed a five-story self-centering concrete frame structure and established a numerical model using OpenSees software. They compared the nonlinear dynamic responses of structures under four sets of seismic motions at different site conditions and conducted collapse risk assessments. Dai et al. [10] established a nonlinear numerical model for a seismic self-centering frame with an infill wall. The incremental dynamic analysis showed that the inter-storey shear of the frame significantly increased after the addition of infill walls, and the maximum inter-storey drift increased by 120.45 %.

Although numerous studies have conducted low-cycle static experiments on self-centering structures, particularly self-centering connections, there is currently a lack of research on the dynamic characteristics and seismic damage evolution of the overall self-centering frame system. Time-frequency analysis is the primary method for the evolution of the frequency characteristics of structures [34]. Hall et al. [35] used a time-frequency method based on wavelet transform to analyse the transient vibration characteristics of a 2×2 pile group model in a shaking table test. Compared with traditional Fourier analysis, the advantage of this method is that it can effectively visualise the change in the structural frequency and frequency content of the ground motion caused by liquefaction over time. Yuan et al. [36] proposed an improved time-frequency analysis method based on the generalised S-transform to improve the accuracy of structural instantaneous frequency identification. Numerical simulations and experimental results demonstrate that this method can effectively identify the structural frequency of nonstationary response signals with high accuracy and good stability. Mohebi et al. [37] proposed complex Morlet wavelet-based refined damage-sensitive feature to study the seismic collapse capacities of RC moment resisting frames (MRF). Through numerical simulation with OpenSees, it has been validated that the proposed method can accurately predict seismic damage to such structures. Yazdanpanah et al. [38] developed a new algorithm to map the fragility curves in adjacent MRFs through improved wavelet-based refined damage-sensitive feature. The research results indicated that this algorithm can locate and evaluate complex nonlinear damage. For MRF structures at different storeys, it can predict their impact and seismic damage states. These studies focused only on the recognition of time-frequency signals and did not study the frequency change state of the structure, nor did they establish the relationship between the time-frequency change and the specific nonlinear state of the structure.

The development of machine learning (ML) technology has brought new possibilities for studying the dynamic characteristic changes of complex structures, especially the prediction of seismic response and damage probability of structures, which has great potential [39]. Kazemi et al. [40–43] quantified the uncertainty into the seismic risk assessment of reinforced concrete (RC) structures, conducted a series of studies on RC structures and SMRF structures, and carried out vulnerability assessments. The results showed that the data-driven methods for structural response prediction solved the problems of computationally expensive, time-consuming, and complex analysis that exist in the current traditional methods. XGBoost and random forest (RF) had higher prediction accuracy and were more suitable for structural seismic response prediction. Zhang et al. [44] used statistical-based machine learning and deep learning (DL) methods to predict the seismic response of a two-storey seismic damped steel frame. The research results showed that the DL algorithm based on unsupervised feature extraction had a good structural response prediction accuracy when the structure entered a strong non-linear state, while the accuracy of traditional ML algorithms with manually extracted features were relatively low. With the

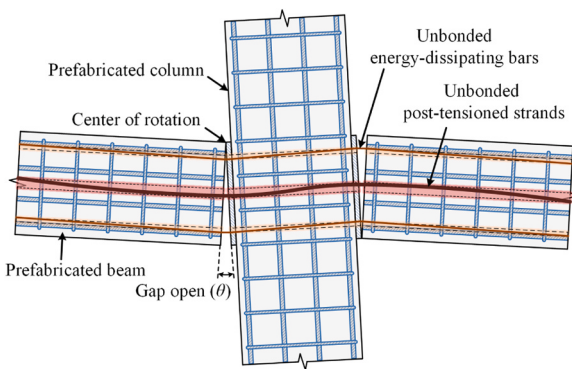


Fig. 1. Deformation of PTHC in gap opening state.

popularity of data-driven methods, especially DL algorithms [45], studying the time-frequency variation of structures and the corresponding nonlinear states is convenient. Lu et al. [46] proposed a rapid post-earthquake damage assessment method for regions based on Convolutional Neural Networks (CNN). Su et al. [47] added a denoising module to the CNN, which denoised the input seismic motion signals and simultaneously carried out damage assessment at the same time. Previous studies have demonstrated the potential of ML for accurate and efficient damage assessment. Ning et al. [48] used long short-term memory (LSTM), WaveNet, and 2D-CNN to predict seismic response time histories of structures, the results showed that the 2D-CNN took STFT-converted spectrograms as the inputs and outputs, which benefited displacement prediction by capturing the associated time and frequency features simultaneously. The literature indicates that CNN algorithms can obtain a larger receptive field by stacking convolutional layers, thereby extracting features from input data. At the same time, CNNs have a certain degree of interpretability, which is an advantage not found in LSTM and Transformer algorithms. For two-dimensional input features such as time-frequency, CNNs are more suitable for processing these types of signals.

In summary, current research on self-centering structures mostly focuses on conducting experiments and finite element analysis on its static mechanical behavior. There is a lack of analysis on the dynamic characteristics of self-centering frame structures. This study uses synchrosqueezing transformation to analyze the frequency evolution of self-centering structures. Then, a CNN model is used to establish the relationship between frequency evolution characteristics and damage state. Finally, a convolution explanation method based on gradient information is used to interpret the content extracted by the CNN.

2. Prototype structure and ground motion selection

2.1. Prototype self-centering structure

The precast self-centering concrete frame (PSCCF) investigated in this study was prestressed using post-tensioning (PT) method, in which the prefabricated concrete members were connected by dry joints, and the connection areas were denoted as hybrid connections. In typical post-tensioned hybrid connections (PTHCs) [24], prefabricated beams and columns are compressed by unbonded PT strands, and the unbonded part of the energy-dissipating bars (EDBs) built into the prefabricated beams exerts energy-dissipating effects through tensile and compressive yielding mechanisms. PTHCs rely on the squeezing effect of prestress to resist the shear force generated by the friction force on the beam-column contact surface. Fig. 1 shows the working state of the PTHC. With an increase in the drift of the connection, the contact surfaces of the beam and column gradually gap. The entire PTHC rotated around the upper and lower rotation centers of the beam, and the built-in unbonded EDBs dissipated energy.

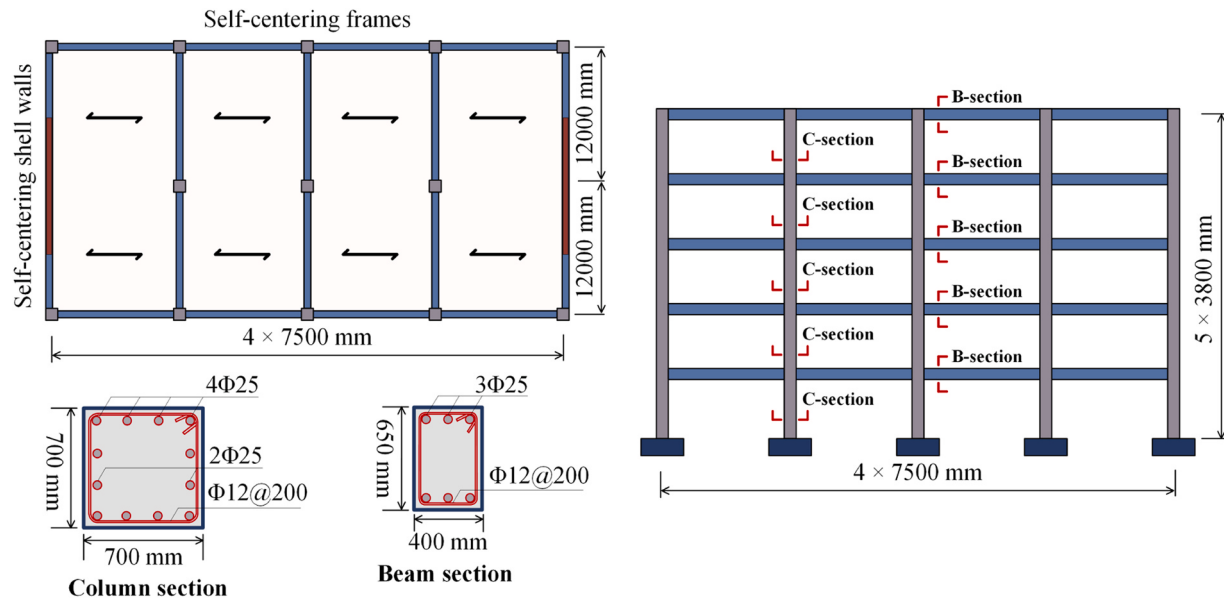
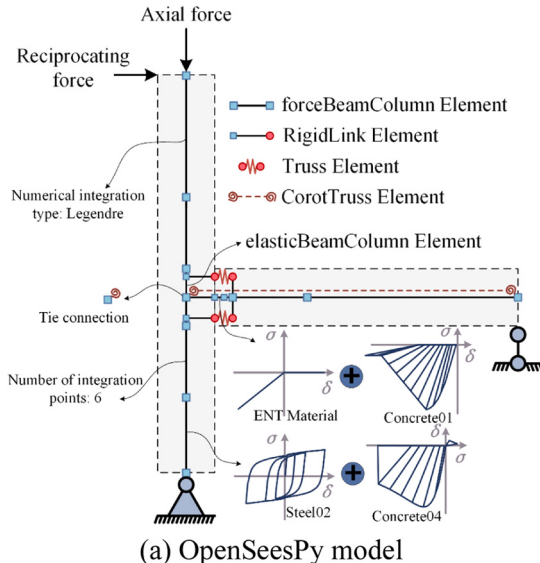


Fig. 2. Prototype self-centering structure.



(a) OpenSeesPy model

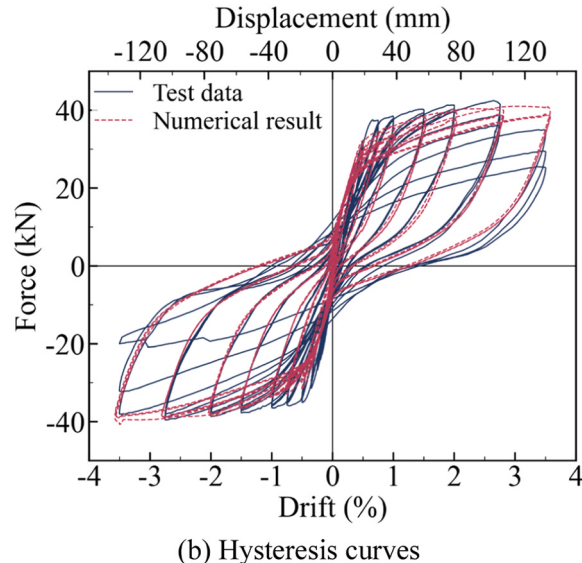


Fig. 3. Modeling calibration of the PTHC.

A five-story PSCCF structure designed according to the PRESSS Design Handbook, located in Wellington, New Zealand, was selected as the prototype model for this research [49]. The plane length of the prototype structure was 30 m, and its width was 24 m. Self-centering shear walls were set in the transverse direction of the structure to ensure seismic resistance. Therefore, a one-bay longitudinal frame containing only PTHCs was selected as the structure for analysis in this study, as shown in Fig. 2. The analysed structure was a one-bay, four-span, five-story PSCCF structure with 7.5 m per span and 3.8 m storey height. The columns had a cross-section of 700 mm × 700 mm, the beams had a section of 650 mm × 400 mm, and the thickness of the protective layer of concrete was 30 mm. The nominal compressive strength of the concrete in the beams and columns was 40 MPa, and the nominal yield strength of the steel bars was 400 MPa. The yield strength of the prestressed steel strands was 1560 MPa, and that of the unbonded EDBs was 300 MPa.

2.2. Numerical model and nonlinear static analysis

Fig. 3 illustrates the FE model developed for the PTHCs. Based on the experimental results [24] of the PTHCs, the OpenSeesPy [50] framework was used to establish a numerical model of the hybrid connection to validate the modelling approach, and the same modelling method was then applied to the PSCCF structure. As shown in Fig. 3(a), the beam and column were modelled using a force-based nonlinear beam element, except for the core of the connection, which was modelled using an elastic beam element. Each segment of the nonlinear beam was integrated using the Gaussian-Legendre integration method with six integration points. In the fibre section of the nonlinear beam element, uniaxial Giuffre-Menegotto-Pinto steel (Steel02) was used to simulate the longitudinal reinforcement, and Popovics concrete (Concrete04) was used to simulate the nonlinear behaviour of the concrete. Uniaxial elastic-no tension (ENT) material and uniaxial Kent-Scott-Park concrete (Concrete01) material were used to establish a fibre section that only bore the pressure at the contact position of the beam and column to

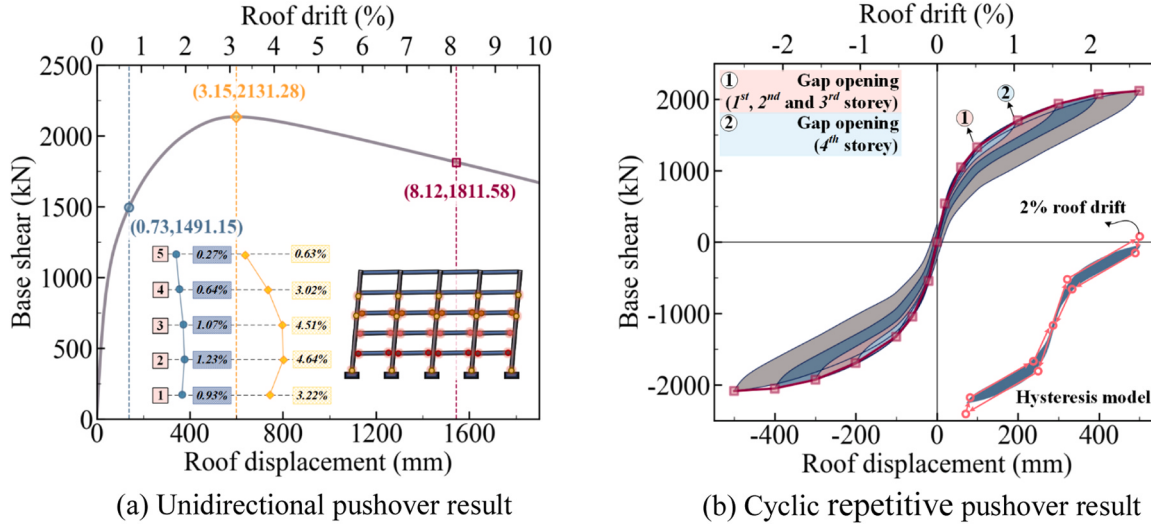


Fig. 4. Static analysis results of the PSCCF.

simulate the gap opening of the connection. Unbonded EDBs were simulated using a truss element and connected to the beam and column using the RigidLink element. The PT strands were simulated using the CorotTruss element and shared the same joints with the beam elements to simulate the tie connections. A hinge was placed at the bottom of the column, and a double hinge was placed at the beam end. Static loading was reciprocated by applying axial pressure to the top of the column. The unbonded EDBs had a yield strength of 554 MPa, an unbonded length of 60 mm, and a diameter of 16 mm. The concrete had a compressive strength of 41.22 MPa with a peak strain of 0.002. The PT strands had a yield strength of 1720 MPa, a cross-sectional area of 560 mm², and an initial prestress of 281 kN. A comparison of the hysteresis curves obtained from the numerical analyses and experiments is shown in Fig. 3(b). The results show that the numerical model can accurately predict the hysteresis behaviour of the hybrid connection. Therefore, in the subsequent analysis of the self-centering frame, the above modelling method was also adopted for the connection part.

The damping ratio of the PSCCF model was set to 5 %, and the first-to-third-order periods were 1.37 s, 0.42 s, and 0.22 s, respectively. As the mass of the main vibration mode exceeded 75 % of the total mass, an inverted triangular distribution lateral force pattern was used to apply a lateral force to the model. The PSCCF was statically pushed up to 10.0 % of the roof drift (ratio of the average displacement at the top of the structure to the overall height). The base shear versus roof drift curve is shown in Fig. 4(a). The yield roof drift of the PSCCF model was calculated as 0.73 % using the farthest point method, and the drift corresponding to the maximum base shear force was 3.15 %.

Under the action of the initial prestress, the beam and column sur-

faces were tightly fitted. As the drift increased, the PSCCF system joined the decompression stage and finally opened the contact surface. The pressure-eliminating drift (θ_{dec}) of each storey is calculated as Eqs. (1–2):

$$M_{dec} = F_{PT} \frac{H_{beam}}{6} \quad (1)$$

$$\theta_{dec} = \frac{M_{dec} L_{beam}}{3E_c I_{beam}} \quad (2)$$

where H_{beam} is the height of the precast beam, L_{beam} is the distance from the contact surface of the beam end to the contraflexure point, E_c is the elastic modulus of the concrete, and $E_c I_{beam}$ is the effective stiffness of the beam. θ_{dec} calculated to be 0.63 % under the design conditions of this research. The maximum inter-storey drift (1.23 %) appeared on the second storey when the structure entered the yield state. The gap-opening phenomenon occurred at the PTHCs of the 1st to 4th storeys of the PSCCF. With an increase in the roof drift of the structure, when the base shear reached the peak force, the EDBs of all storeys entered the energy-dissipating state. Fig. 4(b) illustrates the total base shear versus roof drift curve under cyclic loading of the PSCCF model. According to the hysteresis curves of the cyclic repetitive pushover, the PSCCF model had low energy dissipation, the EDBs were the main energy-dissipating parts of the structure, and the beams and columns maintained the elastic state under a relatively large roof drift. When the roof drift of the PSCCF reached 0.5 %, gaps were formed at the beam-to-column interface of the connections in the first, second, and third storeys, and the gap of the fourth story opened when the drift reached 1 %. When the drift reached

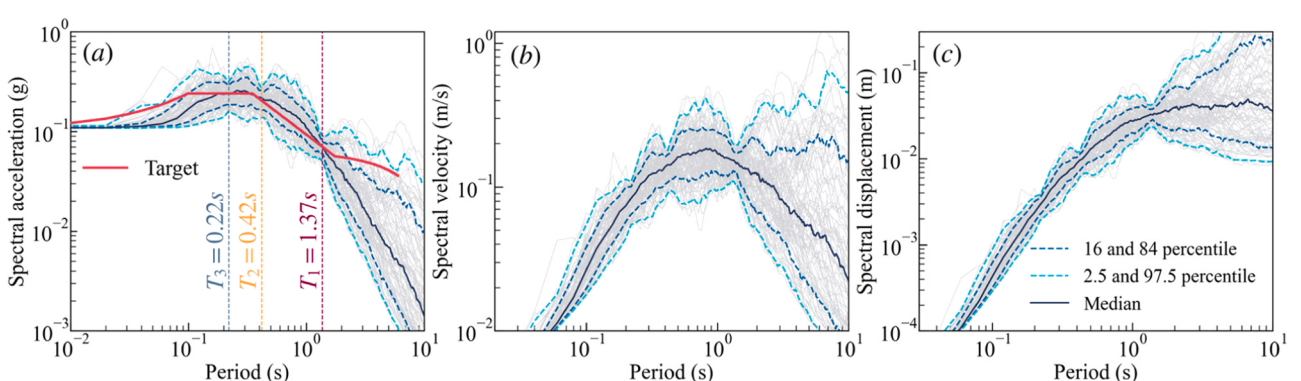


Fig. 5. Response spectrum of ground motion records (5 % damping ratio): (a) acceleration, (b) velocity, and (c) displacement.

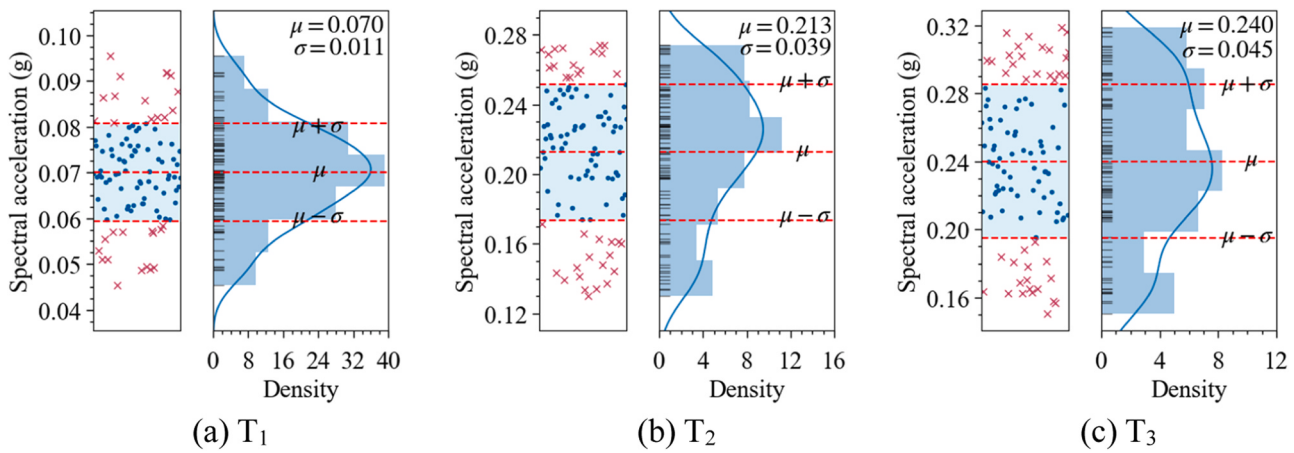


Fig. 6. Frequency distribution of ground motion records at T_1 , T_2 , and T_3 .

2.5 %, the residual deformation rate of the overall structure was 0.26 %, and the frame exhibited a strong self-centering ability.

The hysteresis loop at 2 % roof drift exhibited an ideal double-flag shape. The hysteresis model was multistage elastic, and the stiffness of the PSCCF was a two-stage stiffness. The above analysis results show that the nonlinearity of the self-centering frame is caused by the gap opening at the beam–column interface. The entire structure remained elastic, and its hysteresis properties were restored.

2.3. Ground motion selection and characteristics

A total of 100 natural ground motions were selected from the PEER ground motion database [51] according to the target response spectrum of class II sites under 8 degree frequent earthquakes specified in GB 50011–2010 [52], and the peak ground accelerations (PGA) were modulated on this basis. First, PGA was adjusted to 0.108 g for all ground motion records, and the spectral accelerations of control periods (i.e., T_1 , T_2 and T_3) were calculated. The spectral acceleration values of 100 ground motions at control period T_1 presented a normal distribution around the standard spectrum and the error of the spectral accelerations between the ground motions and standard was ensured to be within 35 % for the three control periods.

The acceleration, velocity, and displacement spectra ($S_{a,5\%}$, $S_{v,5\%}$ and $S_{d,5\%}$) of all the selected ground motion records are shown in Fig. 5. The median value of the $S_{a,5\%}$ of the ground motions was very close to the target value in the three control periods. Fig. 6 illustrates the frequency distribution of the ground motion records at T_1 , T_2 and T_3 control periods. $S_{a,5\%}$ at the fundamental period had a mean value (μ) of 0.07 g and a standard deviation (σ) of 0.01 g, which approximated a normal

distribution. The mean values at T_2 and T_3 were distributed as 0.21 g and 0.24 g with an error of less than 5 % compared to the target.

Incremental dynamic analyses (IDA) were carried out for the PSCCF model, with the PGA of each ground motion record from 0.01 g to 1.0 g incrementally increased at the rate of 0.1 g. Structural hazard levels of immediate occupancy (IO), life safety (LS), and collapse prevention (CP) were adopted from FEMA 356 [53], and the threshold values of maximum inter-storey drift (θ_{\max}) for IO, LS and CP were defined as 1 %, 2 % and 4 %, respectively. Through IDA analysis, the frequency evolution characteristics of the structure and the component response were statistically analyzed, and the dynamic characteristics evolution law of PSCCF under different PGAs was further obtained, and the mapping relationship between dynamic characteristics and structural damage was established. The calculation method of dynamic characteristics and the seismic response of the structure will be explained in the next section.

3. Time-frequency and seismic response analysis of PSCCF

The evolution of dynamic characteristics of PSCCF is mainly characterized by time-frequency states. In this section, the selected seismic waves are used for amplitude modulation and nonlinear time-history analysis of PSCCF is carried out. The time-frequency evolution of PSCCF, the deformation state of PT strands and EDBs, the probability of inter-storey deformation and collapse are further investigated.

3.1. Wavelet analysis technique

The continuous wavelet transform (CWT) overcomes the disadvan-

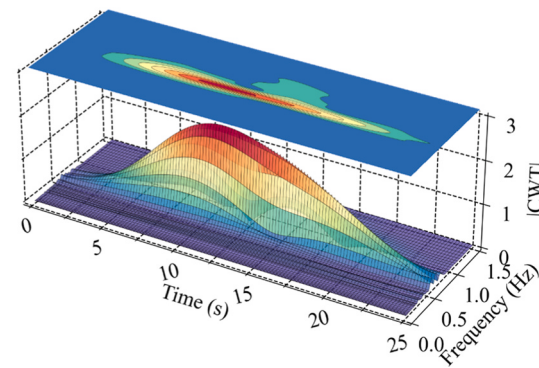
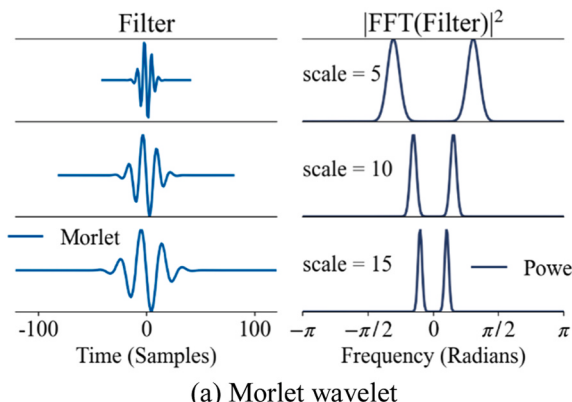


Fig. 7. Continuous wavelet analysis.

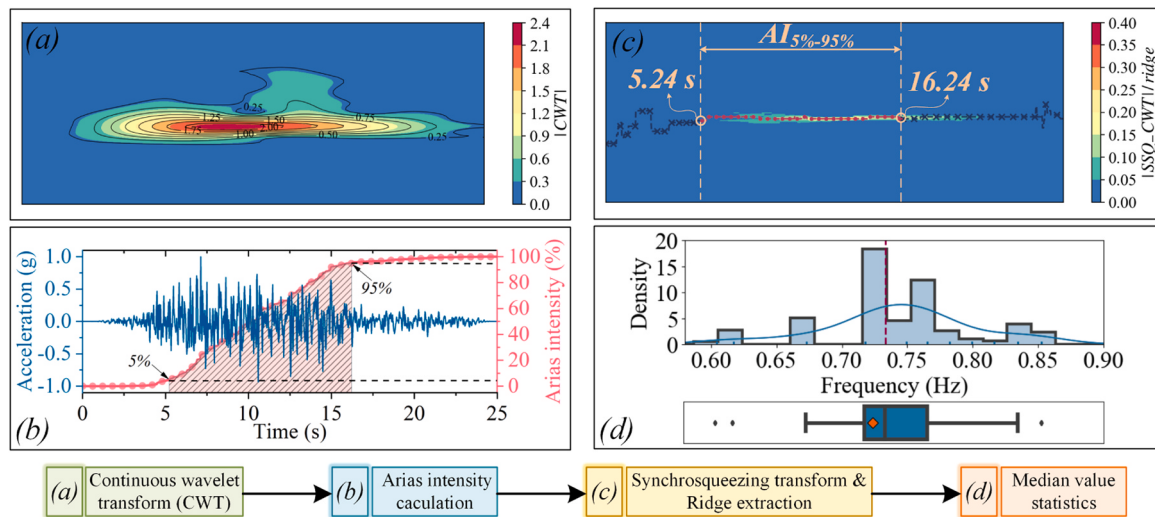


Fig. 8. Frequency statistics process.

tage that the window size does not change with frequency and calculates the frequency change of the signal with time by changing the scale and translation of the wavelet basis function. The parent wavelet in this study was the Morlet wavelet, which is defined by Eq. (3):

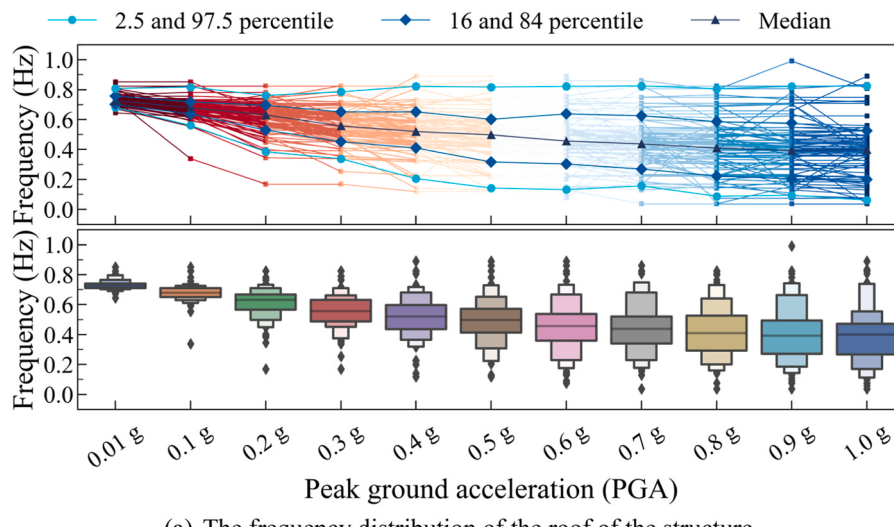
$$\psi(t) = e^{-t^2/2} e^{i\omega_0 t} \quad (3)$$

where, ω_0 represents the scale of the wavelet, which is inversely pro-

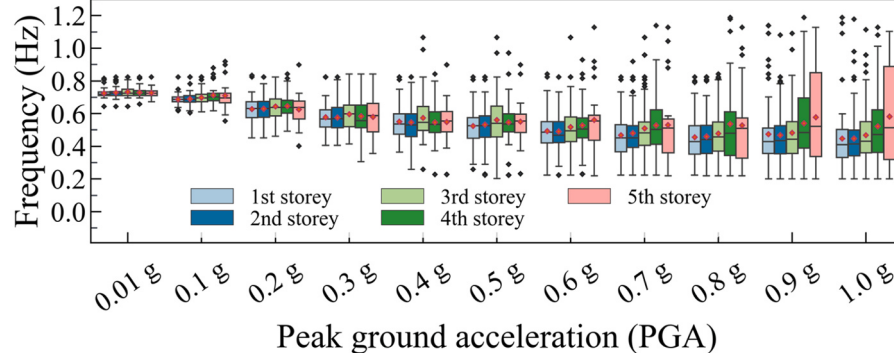
portional to the frequency of the signal, as shown in Fig. 7(a). In the time domain, CWT was performed on the seismic response of the PSCCF, as shown in Eq. (4):

$$CWT(a, b) = \frac{1}{\sqrt{a}} \int_{-\infty}^{+\infty} f(t) \psi\left(\frac{t-b}{a}\right) dt \quad (4)$$

where $f(t)$ is the seismic response signal, a is a scalar parameter, and b is



(a) The frequency distribution of the roof of the structure



(b) The frequency distribution of the inter-storey of the structure

Fig. 9. Frequency distribution of PSCCF in $AI_{5\%-95\%}$.

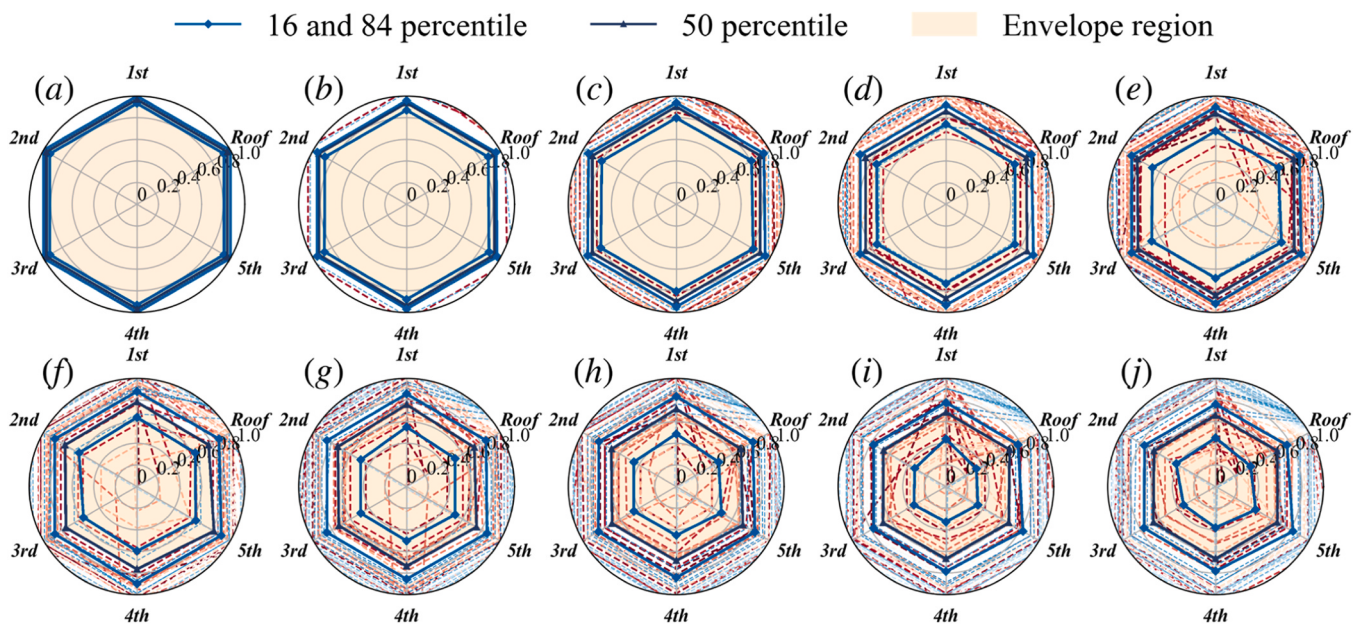


Fig. 10. The frequency distribution of PSCCF in $AI_{95\% \sim 100\%}$: (a) 0.1 g, (b) 0.2 g, (c) 0.3 g, (d) 0.4 g, (e) 0.5 g, (f) 0.6 g, (g) 0.7 g, (h) 0.8 g, (i) 0.9 g, (j) 1.0 g.

the time-shift factor. The essence of the CWT is the integration process of multiplying the parent wavelet and the signal to be analysed. Fig. 7(b) illustrates the time-frequency distribution of the top displacement of the PSCCF when the *PGA* of the ground motion record (1989 Loma Prieta earthquake) was 0.01 g.

3.2. Frequency statistics methods for PSCCF

Although the CWT can obtain the frequency distribution of the input signal, the resolution of the analysis results is low, and the time-frequency aggregation is poor, as shown in Fig. 8(a). By remapping the energy of the CWT results in the time and frequency directions, the CWT coefficients can be mapped to the instantaneous frequency position of the signal, and the frequency analysis of nonstationary signals can be carried out effectively. Synchrosqueezing CWT (SSQCWT) [54] is a time-frequency analysis method with high resolution and aggregation that can represent the instantaneous frequency change of a signal by its good signal reducibility. In the time-frequency plane, the CWT synchrosqueezed results can be calculated using Eqs. (5–6):

$$SSQCWT_f(\xi, b) = \int_{\{a \in R_+, CWT(a, b) \neq 0\}} CWT_f(a, b) \delta(\omega_f(a, b) - \xi) \frac{1}{a} da \quad (5)$$

$$\omega_f(a, b) = -i \frac{\frac{\partial}{\partial b} CWT_f(a, b)}{CWT_f(a, b)} \quad (6)$$

where δ is the Dirac function, ξ is the frequency value. Based on the SSQCWT, the maximum energy time-frequency ridge can be extracted to separate the signals.

For all ground motion records, the time corresponding to an Arias intensity (*AI*) ratio of 5 % to 95 % was calculated as the earthquake duration. The *AI* was calculated as follows:

$$AI = \frac{\pi}{2g} \int_0^{T_d} a(t)^2 dt \quad (7)$$

where g is the acceleration due to gravity, $a(t)$ is the acceleration time of the ground motion, and T_d is the duration of $a(t)$ within the threshold, as shown in Fig. 8(b). The results of the CWT were rearranged and synchrosqueezed, and ridges within the $AI_{5\% \sim 95\%}$ were extracted. Finally, frequency statistics were performed, and the dynamic frequency of the structure was characterized by the median frequency value, as shown in

Fig. 8(c) and (d).

3.3. Frequency distribution of PSCCF

Statistical frequency response of maximum probability density of structure under each ground motion record. Fig. 9 illustrates the frequency distribution of the roof and inter-storey of the PSCCF structure. The variation in structural frequency under amplitude-modulated seismic excitation is shown in Fig. 9(a). The 2.5 %, 16 %, 50 %, 84 %, and 97.5 % quantiles of statistical frequencies are shown in the figure. In general, as the *PGA* of the seismic excitation increased, the frequency at the top of the structure decreased constantly. Using SSQCWT to statistically obtain the frequency with the maximum probability distribution of the structure under each excitation's *PGA* of 0.01 g, and then calculating the median value of all frequencies as 0.725 Hz, which was very close to the fundamental frequency of the PSCCF (0.729 Hz), this also verified the accuracy of the SSQCWT algorithm.

When the *PGA* of the input ground motions was 0.1 g, the median frequency of the structure was 93.77 % of the initial fundamental frequency. At this point, the beam-column connections of the PSCCF had almost no gap openings. However, when *PGA* reached 0.5 g, the median frequency was only 68.65 % of the first-order frequency, and the structure exhibited evident nonlinearity. When the *PGA* reached 1.0 g, the frequency of the structure was 55.10 % of its initial fundamental frequency. As *PGA* increases, the rate of decline in the structure frequency tends to decrease. The statistical results in Fig. 9(a) indicate that the structure has a relatively fixed interval length with a higher probability density in the $AI_{5\% \sim 95\%}$. This is also evidenced by the box plot, which shows a smaller dispersion of the interval frequencies within the 16–84 percentiles. In most cases, when the *PGA* of the ground motion was 0.1 g, the frequency distribution interval is predominantly within 0.64–0.72 Hz. As the *PGA* increased to 0.5 g, this interval decreased to 0.32–0.60 Hz. With a further increase in *PGA* to 1.0 g, the distribution interval became 0.20–0.53 Hz. Overall, once the structure enters nonlinearity, the interval error of its frequency concentration is approximately 0.3 Hz. Relative to the upper and lower limits of the PSCCF frequency range, the statistical results indicated that the interval between $AI_{5\% \sim 95\%}$ frequencies was relatively small. This suggests that the frequencies of PSCCF that occurred during the earthquakes were highly concentrated.

Fig. 9(b) illustrates the statistical results of the inter-storey vibration

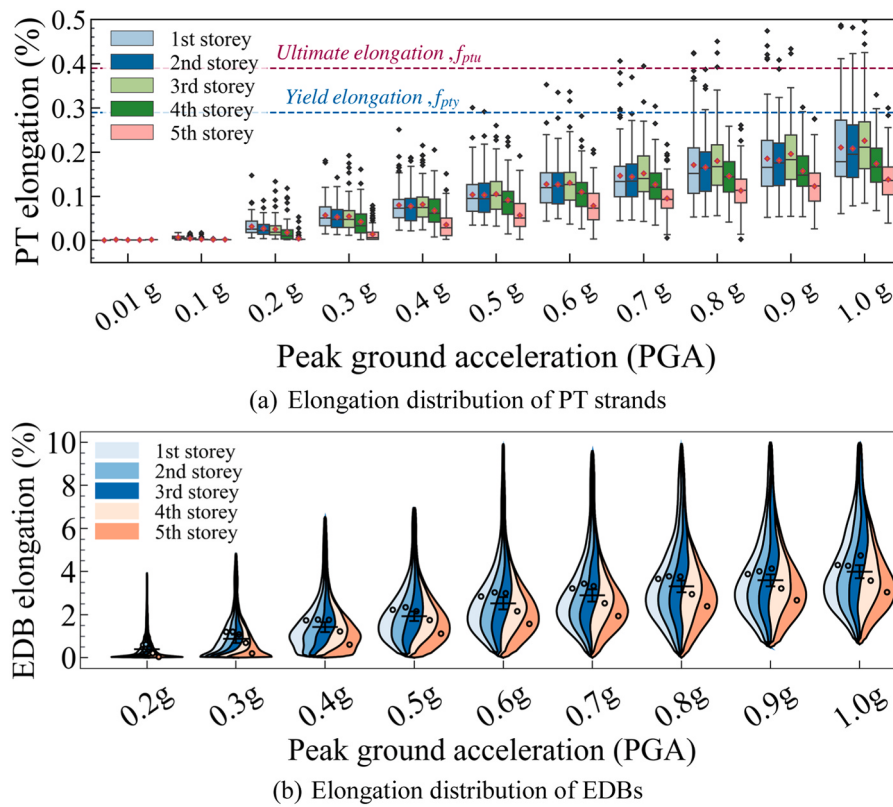


Fig. 11. Elongation distribution of PT strands and EDBs.

frequencies of each story of the PSCCF under different PGA of the ground motions. Overall, the inter-storey variation frequency trend of each story of the PSCCF was similar to the roof frequency, and the fundamental distribution frequency of each story gradually decreased. At a PGA of 0.01 g, the mean inter-story vibration $AI_{5\%-95\%}$ frequency of the structure was 0.724 Hz, which was close to the fundamental frequency of the PSCCF. When the PGA was less than 0.5 g, the inter-story frequencies of the PSCCF decreased rapidly, with an average frequency reduction rate of 25.87 %. However, when the PGA was greater than 0.5 g, the frequency decrease of the fourth and fifth storeys slowed down, while the median frequencies of the first three storeys still showed a fast downward trend. When the PGA reached 1.0 g, the $AI_{5\%-95\%}$ frequency reduction of the first to third storeys of the structure exceeded 40 %, and the reduction rates of the fourth and fifth storeys were 34.89 % and 29.06 %, respectively.

The statistical analysis of the $AI_{5\%-95\%}$ seismic excitation reflects the frequency distribution characteristics of the structure during an earthquake. After the AI exceeded 95 % ($AI_{95\%-100\%}$), the energy of the seismic excitation decreased significantly, and the frequency distribution of the PSCCF approached the post-seismic frequency. Fig. 10 shows the frequency distribution of the PSCCF in $AI_{95\%-100\%}$ when PGA increased stepwise from 0.1 g to 1.0 g. The radial direction represents the ratio of the story or roof frequency of the structure to its initial fundamental frequency. The blue lines represent the 6 and 84 percentiles, and the black line is the median value of the frequency distribution in $AI_{95\%-100\%}$. The envelope area of the radar chart reflects the frequency reduction rate of the structure in the $AI_{95\%-100\%}$, which reflects the frequency recoverability of the PSCCF. When PGA was less than 0.3 g, the frequency of the PSCCF was recoverable. At this time, the median and 16 and 84 percentile lines almost coincided, and the

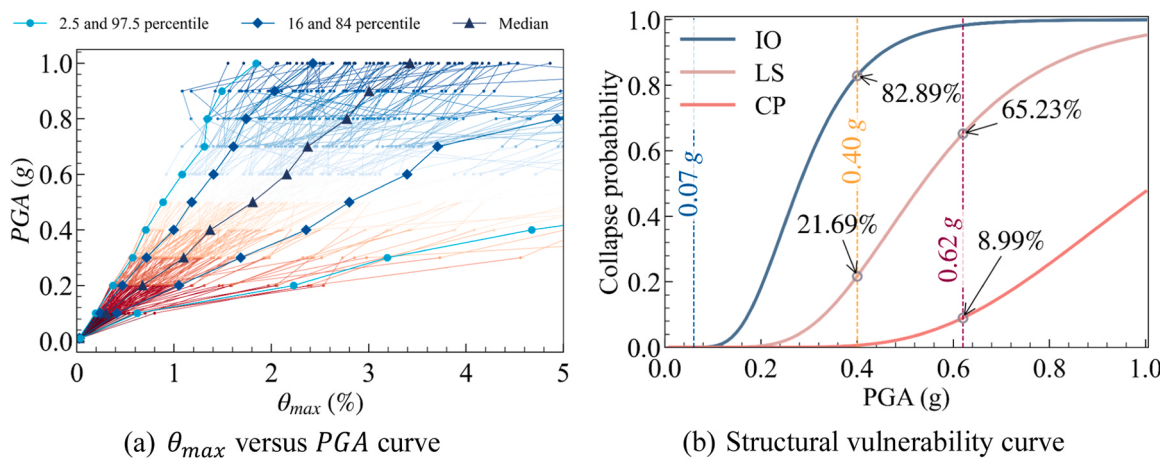


Fig. 12. Incremental dynamic analysis results.

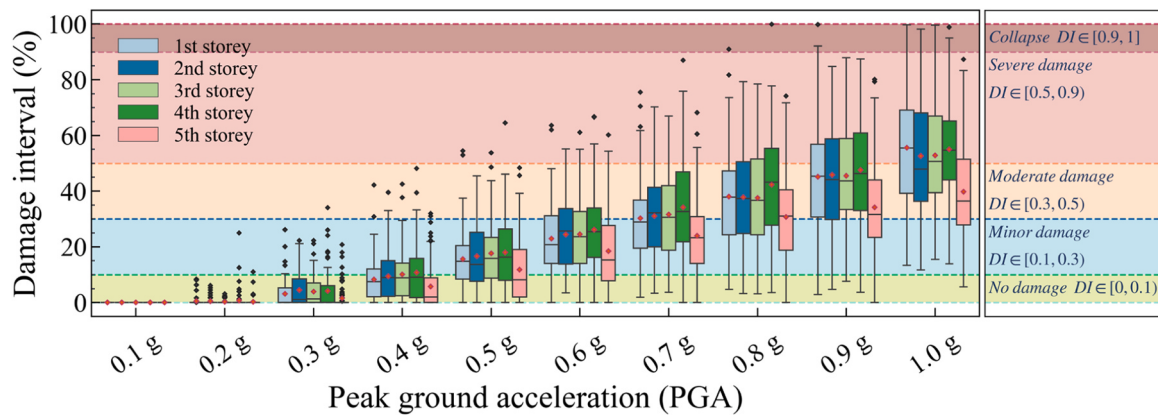


Fig. 13. Damage interval distribution of each storey.

envelope area was full. When PGA reached 0.5 g, the structure exhibited strong nonlinearity and the final frequency degraded, but the median value of the frequency ratio remained above 0.8. When PGA was greater than 0.6 g, the median value of the frequency ratio decreased significantly with an increase in PGA . After PGA reached 1.0 g, the frequency envelope area of $AI_{95\% \sim 100\%}$ was only 40 % of the initial state.

3.4. Structural response of PSCCF

The yield and ultimate elongation rates of the PT strands were 0.29 % and 0.39 %, respectively, and the PT elongation rate in the PSCCF is shown in Fig. 11(a). When the PGA of the seismic acceleration was less than 0.2 g, the joints between the beams and columns had not yet opened, and the prestress did not show a significant change at this time. However, as the PGA content increased, the elongation rate of the PT strands in the structure increased significantly. Overall, the change in prestress in the first three storeys was more significant than in the fourth and fifth storeys. When the PGA exceeded 0.5 g, the PT strands in some storeys yielded. However, overall, the median value of the maximum elongation rate at 0.5 g was 0.11 %, and the prestress of the structure was within a safe range under the design earthquake. Even under a PGA of 1.0 g, the median value of the maximum elongation rate of the structure was 0.21 %, which is safe under rare earthquakes. The yield elongation rate of EDB was 0.15 %. When the PGA exceeded 0.3 g, the EDBs on the first three storeys of the structure entered the energy-dissipating phase. At this time, the median value of the elongation rate of the EDBs at the top floor was less than 1 %, consistent with the PT strands, and no gap openings appeared in the connections at the top storey. When the PGA of the PSCCF reached 1.0 g, the median value of the maximum elongation rate of the EDBs was 4.37 %, which is still less than the maximum elongation rate limit of 7 % required by the specifications [55], as shown in Fig. 11(b).

The incremental dynamic analysis results of the PSCCF are shown in Fig. 12. As the PGA increased, the maximum inter-storey drift (θ_{max}) of the structure continued to rise, the median value of the θ_{max} of the structure was 0.68 % when the PGA was 0.2 g, at which point some storeys had just begun to appear gap opening. When the PGA increased to 0.5 g, the median value of the θ_{max} increased to 1.81 %. The structure entered a stronger nonlinear state but was still within the LS target control. Even when the PGA continued to increase to 1.0 g, the θ_{max} of the structure was 3.42 %, which was still within the target range of CP defense, as shown in Fig. 12(a). The vulnerability curves of the PSCCF were plotted with PGA as the horizontal axis and the probability of exceeding the limit state as the vertical axis. These curves were fitted using a lognormal distribution function, as shown in Fig. 12(b). Under frequent earthquakes, a PSCCF can be used immediately. The probability of the structure exceeding the LS level under a 8 degree rare earthquake was 21.69 %, and the probability of the structure exceeding

the CP level under a 9 degree rare earthquake was 8.99 %. This indicates that the PSCCF had good anti-collapse capabilities.

The dynamic nonlinear response of PSCCF was closely related to its frequency evolution. When PGA was less than 0.2 g, the elongation rate of unbonded energy-dissipating bars changed very little, and the frequency of the structure was close to the initial frequency. After PGA exceeded 0.2 g, the IO exceedance probability of the structure began to rise. When PGA exceeded 0.4 g, the collapse probability increased, and the post-seismic frequency of PSCCF became irrecoverable. When PGA exceeded 0.6 g, the growth rate of the elongation rate of PT strands and energy-dissipating bars slowed down. At this time, the frequency change of the PSCCF was also small, and the structure entered an obvious nonlinear state.

4. Structural damage prediction based on DL algorithm

The time-frequency characteristics of the PSCCF varied significantly with different ground motions. However, as the PGA increased, the primary frequency decreased, whereas the degree of damage to the structure increased. Therefore, an intrinsic connection exists between the time and frequency of the structure and its damage interval (DI).

4.1. Damage model applied to PSCCF

This study used the damage model proposed by Kunnath et al. [56], which is defined as Eqs. (8–10):

$$DI = DI_{\theta_c} + DI_{\int dE} \quad (8)$$

$$DI_{\theta_c} = \frac{\theta_m - \theta_r}{\theta_u - \theta_r} \quad (9)$$

$$DI_{\int dE} = \beta \frac{\int dE}{M_y \theta_u} \quad (10)$$

where θ_m and θ_r are the maximum deformation and recoverable deformation during ground motions, θ_u is the ultimate deformation capacity under monotonic loads; M_y is the yield moment of hybrid connections, and β is a non-negative parameter related to energy-dissipation capacities. Based on the regression results of the sub-item coefficients of the hybrid connections damage energy by Zhou et al. [29], the value of β was taken as 0.0742. The deformation and hysteresis energies under the seismic action were calculated for each storey, and the damage interval distribution for each story of the PSCCF was calculated, as shown in Fig. 13.

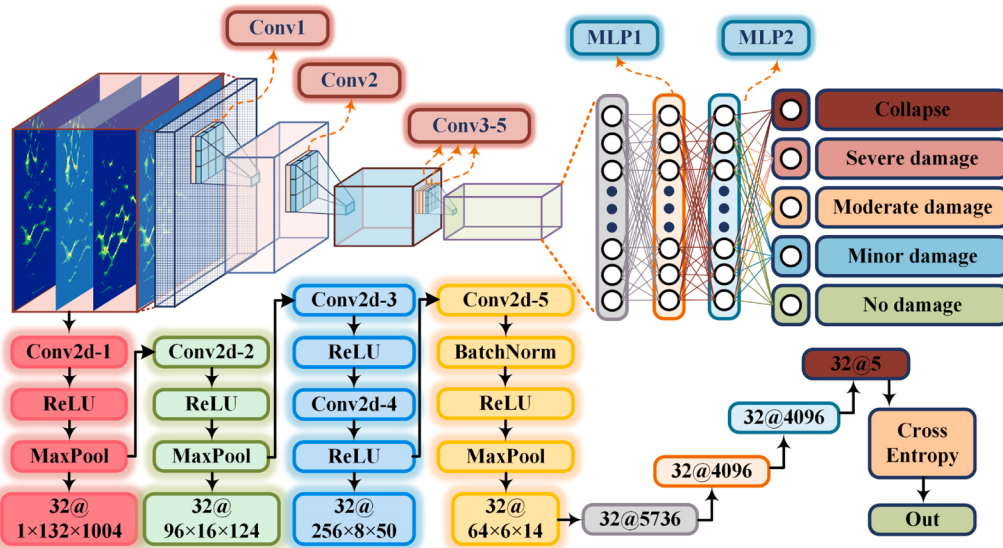


Fig. 14. Convolutional neural network structure diagram.

4.2. Prediction method from time-frequency to structural damage state

Although the damage state of a structure can be obtained through the deformation of the structure and hysteresis energy during an earthquake, the energy index must be calculated using the force-time history. However, in practical engineering applications, it is difficult to monitor this index. Therefore, developing a faster and more intuitive damage state prediction method for PSCCF is necessary. Deep learning (DL) technology can establish time-frequency signals that are easier to monitor, thereby predicting the damage interval of a novel structure.

This study used a convolutional to map the input time-frequency signals, thereby establishing its relationship with the structural damage state. The algorithm structure and tensor-dimension changes used in this study are shown in Fig. 14. By padding the input time-frequency signals with zeros, the characteristic dimension of each time-frequency was kept the same. The input features of this study were 5500 time-frequency signal graphs of the SSQCWT. These signals were processed using cross-validation, divided into 10 batches, with 90 % of each batch served as the training dataset and the remaining 10 % as the testing dataset. The input batch size was 32, and the dimensions of each signal were $1 \times 132 \times 1004$ as a result of signal downsampling. Five convolutional layers are used to map the input features, thereby compressing the width of the signal and expanding its depth. Subsequently, the results of the convolutional mapping were unfolded and passed into the multilayer perceptron (MLP) layer, finally regressing the probabilities of occurrence of the five damage modes. The cross-entropy loss function was selected as the objective function, and the model weights were adjusted through backpropagation. The cross-entropy loss function

is defined as follows:

$$\text{loss}(x, \text{class}) = -\log \left(\frac{e^{x_{\text{class}}}}{\sum_j e^{x_j}} \right) = -x_{\text{class}} + \log \left(\sum_j e^{x_j} \right) \quad (11)$$

where x is the predicted outcome, and class denotes the actual label of the sample. In the CNN structure, introducing pooling and batch normalization layers enhanced the convergence of the network. Additionally, the inclusion of dropout layers in the MLP layers further improves the generalization capabilities of the algorithm, thereby reducing the risk of overfitting.

4.3. Prediction results analysis

Owing to the black-box effect of deep learning, the mapping operation inside the network is often ambiguous. In this study, gradient-weighted class activation mapping (Grad-CAM) [57] and gradient-shape methods [58] were used to describe deep learning networks. Grad-CAM technology was used to generate visual interpretations of deep neural networks, which can make the models more transparent. Grad-CAM uses the gradient of any object concept and flows it into the last convolutional layer to produce a rough positioning map highlighting the areas of an image that are important for predicting that concept. Fig. 15 illustrates the time-frequency characteristics corresponding to the four damage modes of the PSCCF. As the degree of structural damage increased, the time-frequency oscillations of the structure increased significantly. The convolutional layer focuses more on the lower-frequency parts. As shown in Fig. 15(d), a larger number of

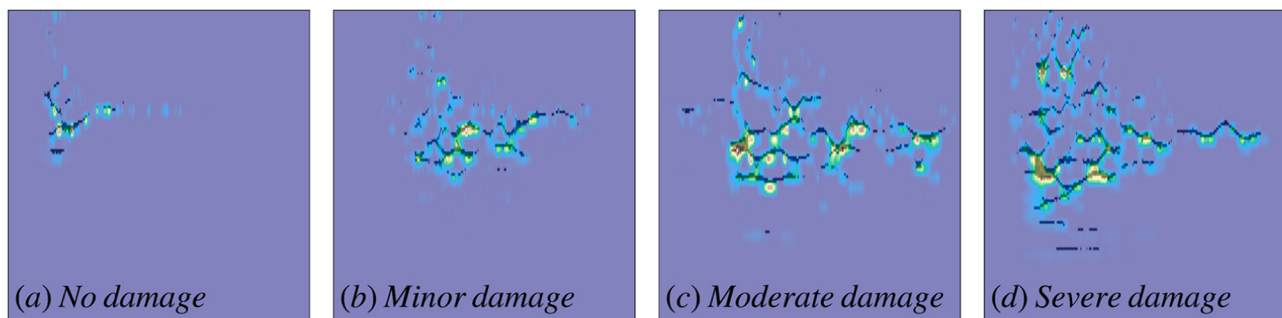


Fig. 15. Gradient-weighted class activation mapping analysis.

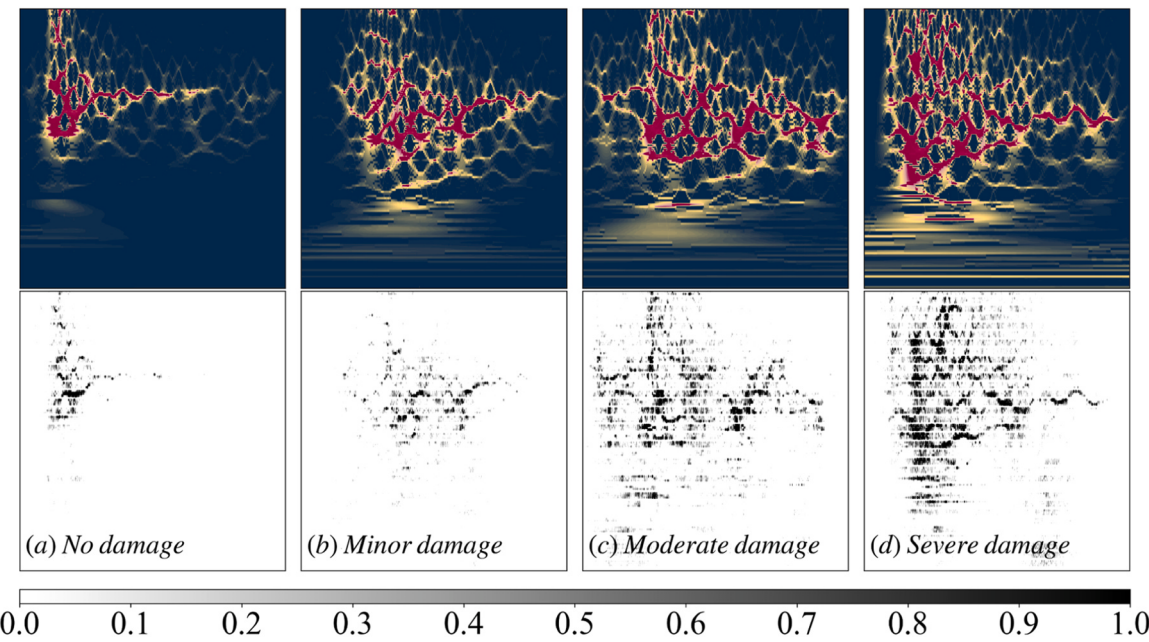


Fig. 16. Gradient-shap interpretability analysis.

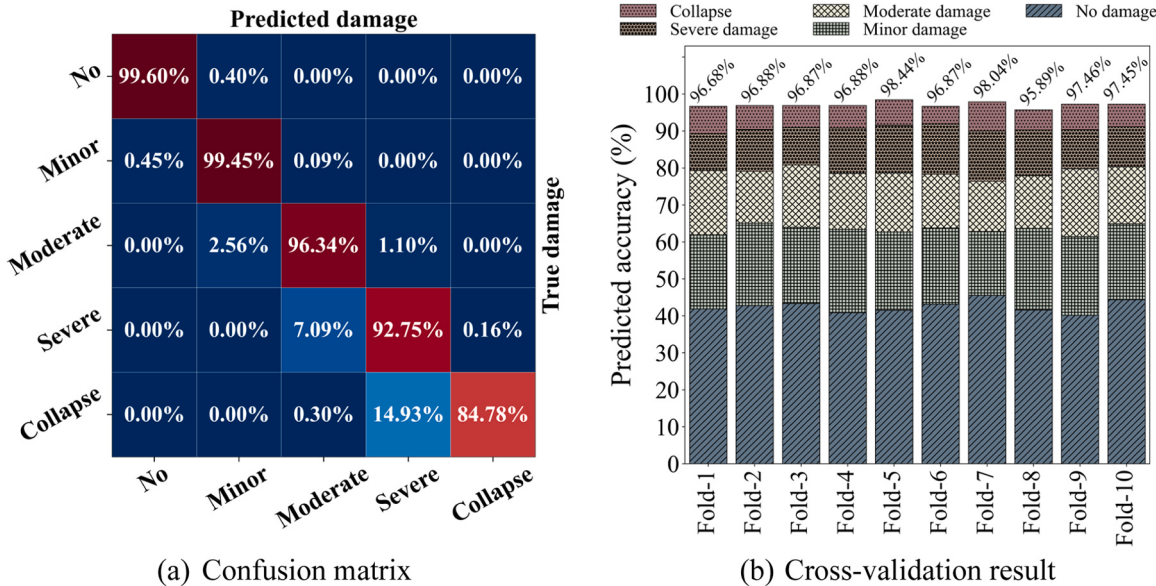


Fig. 17. Deep learning classification accuracy.

low-frequency components are marked with deeper colors, which indicates the occurrence of damage to the PSCCF in the algorithm.

Gradient-Shap is a method for interpreting the predictions of deep neural networks that assign the importance of input features to each prediction based on the Shapley additive explanation values (SHAP) concept. Gradient-Shap uses gradient information combined with random sampling and expectation calculations to estimate the contribution of each feature to the prediction. The gradient gap in this study approximated the SHAP value by randomly sampling the expected gradient from the baseline distribution in the time-frequency features and calculating the output gradient relative to these selected random points, as shown in Fig. 16. The red portion represents the more prominent frequency components in the original signal. In contrast, the gold portion corresponds to less significant frequency components. Fig. 16(a-d) also indicates that not all parts of the time-frequency signal

contribute to predicting structural damage. CNN uses frequencies with larger synchronous compression transform amplitudes as predictive features among most frequency components. This is consistent with the earlier concept of statistically determining the most likely frequency.

The confusion matrix is a situation analysis table summarizing the prediction results and records in the dataset according to the real category and category judgment predicted by the classification model, as shown in Fig. 17(a). Each column of the confusion matrix represents the prediction category, and each row represents the true category of the data. The formula for the confusion matrix is

$$\text{Accuracy} = \frac{TP + TN}{TP + FN + FP + TN} \quad (12)$$

where TP is the true positive class, FN is the false negative class, FP is the false positive class, and TN is the true negative class. For the prediction

Table 1
Seismic IMs for traditional ML algorithms.

IM	Name	Definition
<i>EPV</i>	Effective peak velocity	$\frac{1}{2.5}S_v$ ($T = 1.0$); S_v is the 5 % damped spectral velocity
<i>AI</i>	Arias intensity	$\frac{\pi}{2g} \int_0^{T_{total}} a^2(t) dt$; $a(t)$ is the time history of acceleration
<i>HI</i>	Housner intensity	$\int_{0.1}^{2.5} PS_v(\xi = 5\%, T) dt$; PS_v is the pseudo-spectral velocity
<i>CAV</i>	Modified cumulative absolute velocity	$\int_0^{T_{total}} a(t) dt$
<i>PGA</i>	Peak ground acceleration	$\text{Max} a(t) $
<i>PGV</i>	Peak ground velocity	$\text{Max} v(t) $; $v(t)$ is the velocity time history
<i>PGD</i>	Peak ground displacement	$\text{Max} d(t) $; $d(t)$ is the displacement time history
$S_{ai}(T_1, T_2)$	Spectral acceleration at i s	$S_a(\xi = 5\%, T = i)$; S_a is the 5 % damped spectral acceleration; $i = T_1, T_2$
$S_{vi}(T_1, T_2)$	Spectral velocity at i s	$S_v(\xi = 5\%, T = i)$; $i = T_1, T_2$
S_{amax}	Maximum spectral acceleration	$\text{Max}(S_a)$
S_{vmax}	Maximum spectral velocity	$\text{Max}(S_v)$
<i>Period of S_{amax}</i>	Period corresponding to maximum value of acceleration response spectrum	$T[\text{argmax}(S_a)]$; $\text{argmax}(S_a)$ is the index of maximum spectral acceleration
<i>Period of S_{vmax}</i>	Period corresponding to maximum value of velocity response spectrum	$T[\text{argmax}(S_v)]$; $\text{argmax}(S_v)$ is the index of maximum spectral velocity
S_{amax}/S_{aT1}	Ratio of maximum spectral acceleration to spectral acceleration in first mode period	$\text{Max}(S_a)/S_a(\xi = 5\%, T = T_1)$
S_{amax}/S_{aT2}	Ratio of maximum spectral acceleration to spectral acceleration in second mode period	$\text{Max}(S_a)/S_a(\xi = 5\%, T = T_2)$
S_{vmax}/S_{vT1}	Ratio of maximum spectral velocity to spectral velocity in first mode period	$\text{Max}(S_v)/S_v(\xi = 5\%, T = T_1)$
S_{vmax}/S_{vT2}	Ratio of maximum spectral velocity to spectral velocity in second mode period	$\text{Max}(S_v)/S_v(\xi = 5\%, T = T_2)$
<i>Disp_{max}</i>	Maximum inter-storey deformation of PSCCF	$\text{Max}(\text{Abs}(Disp_{i+1} - Disp_i))$

of structures with no, minor, moderate, or severe damage, the accuracy exceeded 90 %. However, the prediction accuracy of the collapse of structures is relatively low. There are multifaceted reasons for this. First, the proportion of samples with collapse and severe damage was relatively low. This could lead to certain limitations in the training results, failing to encompass all frequency features of collapse. Second, the damage interval for severe structural damage is relatively narrow, indirectly challenging the prediction accuracy. In Fig. 17(b), the proportion of samples for each DI in each cross-validation is marked. As the damage to the structure increased, the number of samples decreased. Overall, the prediction accuracy of the DL model proposed in this study was confirmed to be greater than 95 % through 10-fold cross-validation.

5. Discussion

In this study, CNN was used to extract and fuse features from the time-frequency information of self-centering structures that have undergone SSQ transformation, thereby achieving a satisfactory accuracy in predicting structural damage. The advantage of CNN depended on its unsupervised feature extraction capability, which allowed the network to learn some features that people cannot notice, thereby obtaining a more accurate evaluation of structural damage, which was not possessed by traditional ML algorithms.

Table 2
Comparison of accuracy between DL and traditional ML algorithms.

Algorithm	Precision ratio				
	No damage	Minor damage	Moderate damage	Severe damage	Collapse damage
RC	0.9642	0.3675	0.1765	0.4104	0.7429
LR	0.9432	0.6581	0.5829	0.6045	0.7857
KNN	0.9832	0.8932	0.7807	0.7687	0.8286
SVM	0.9916	0.8889	0.8182	0.7388	0.8429
DT	0.9747	0.8248	0.7861	0.8060	0.8286
RF	0.9684	0.8761	0.8021	0.7164	0.8143
XGBoost	0.9811	0.8803	0.8342	0.7910	0.8571
MLP	0.9684	0.8889	0.7594	0.8657	0.8714
CNN	0.9960	0.9945	0.9634	0.9275	0.8478

This study also used traditional ML algorithms to predict the damage interval of PSCCF, and manually extracted 22 features that may affect structural damage, as shown in Table 1. The research employed seven traditional ML methods based on statistics, namely ridge classifier (RC), logistic regression (LR), k-nearest neighbor (KNN), support vector machines (SVM), decision tree (DT), random forest (RF), and extreme gradient boosting (XGBoost). In addition, a multilayer perceptron (MLP) based on the backpropagation method was also used for comparison. The prediction accuracy of damage interval by these nine algorithms is shown in Table 2. Among the traditional ML methods, XGBoost had the highest prediction accuracy for damage intervals, while the overall accuracy of RC and LR based on linear regression was lower. The accuracy of MLP and CNN was higher than that of traditional ML, and except for the prediction of collapse situations, the prediction accuracy of CNN was higher than that of MLP. The Precision ratio indicated that when there were more training samples, the overall prediction accuracy of CNN was higher than other algorithms. CNN was capable of extracting more comprehensive features. When the structure entered a non-linear state, traditional ML methods were less capable of learning features compared to CNN, which led to a decrease in accuracy.

6. Conclusion

This study established the numerical model of a precast self-centering concrete frame, and IDA analyses were carried out. The dynamic responses and frequency variation of the PSCCF during an earthquake were calculated and statistically analysed. Finally, DL technology was used to predict the damage state of the structure based on time-frequency signals. The main conclusions are as follows.

- (1) The numerical simulation results showed that the numerical model was capable of accurately modeling the cyclic response of the PTHCs, which validates the modelling approach for the PSCCF was acceptable. The cyclic static pushover analysis results of the PSCCF indicated that the envelope curve of the structure approximated a bilinearity, which was caused by the gap opening at the beam-to-column interface. Additionally, the PSCCF exhibited low residual deformation and good recentering capacity, demonstrated typical characteristics of a recoverable functional structure.
- (2) The SSQCWT with a better frequency resolution was applied to the time-frequency variation study of PSCCF subjected to earthquake excitations. The results of frequency analysis showed that when *PGA* was greater than 0.5 g, PSCCF exhibited irreparable damage, resulting in a large decline in its frequency. It was also found that under a *PGA* of 1.0 g, the post-seismic frequency of the PSCCF could only reach 40 % of its initial state.
- (3) The IDA analysis showed that the maximum elongation rates of both the PT strands and EDBs did not change significantly under frequent earthquakes. As *PGA* increased, the EDB of the first three storeys yielded first. The median value of the maximum

elongation rate of PT strands was still in the safe range even when PGA was 1.0 g. PSCCF can be used immediately under frequent earthquakes, and the collapse exceedance probability under rare earthquakes was 8.99 %, indicating that PSCCF had an excellent anti-collapse performance.

- (4) The proposed DL algorithm using time-frequency signals as input features overcomes the shortcomings of traditional damage calculation methods that require calculating structural energy, which is a difficult-to-obtain indicator. The prediction accuracy of the DL algorithm exceeded 95 %. The attention heat map of the CNN was obtained using the Grad-CAM and SHAP methods, indicating that the DL technology also tended to use low-frequency features, and the data-driven results were consistent with the human experience.

It should be noted that the dynamic characteristics of self-centering structures was analyzed in this research, and CNN was used to predict the damage of PSCCF. Although the CNN proposed in this study can make relatively accurate predictions of the damage interval of the structure, neural networks with more hyperparameters are currently flourishing. In the future, more advanced deep learning algorithms will be developed and optimized to predict damage state to self-centering structures.

CRediT authorship contribution statement

Shuguang Wang: Writing – review & editing, Supervision, Project administration, Funding acquisition. **Weizhi Xu:** Writing – review & editing, Supervision, Funding acquisition. **Qisong Miao:** Writing – review & editing, Supervision, Project administration. **Dongsheng Du:** Writing – review & editing, Funding acquisition. **Tianyang Zhang:** Writing – review & editing, Writing – original draft, Software, Investigation.

Declaration of Competing Interest

The authors declare that they have no competing financial interests or personal relationships that may have influenced the work reported in this study..

Data availability

Data will be made available on request.

Acknowledgements

The authors are grateful for financial support from the National Natural Science Foundation of China (52208173), Fellowship of China Postdoctoral Science Foundation (2022M721591), and China-Pakistan Belt and Road Joint Laboratory on Smart Disaster Prevention of Major Infrastructures (2022CPBRJL-09). The authors are grateful for the support from the Jiangsu Funding Program for Excellent Postdoctoral Talents.

References

- [1] Cai XN, Gong N, Fu CC, Zhu YZ, Wu JC. Seismic behavior of self-centering prestressed precast concrete frame subassembly using steel top and seat angles. *Eng Struct* 2021;229:111646.
- [2] Geng FF, Ding YL, Wu HL, Yang JP, Shen W. Seismic performance enhancing of novel self-centering precast concrete frame using replaceable hysteretic dampers. *J Build Eng* 2021;42:103059.
- [3] Huang LJ, Zeng B, Zhou Z, Zhang WQ, Wei Y, Li CY. Seismic behavior and reliability of variable friction damped self-centering prestressed concrete frames considering bolt bearing. *Soil Dyn Earthq Eng* 2023;164:107643.
- [4] Morgen BG, Kurama YC. A friction damper for post-tensioned precast concrete moment frames. *PCI J* 2004;49:112–33.
- [5] Zhao B, Taucher F, Rossetto T. Field investigation on the performance of building structures during the 12 May 2008 Wenchuan earthquake in China. *Eng Struct* 2009;31:1707–23.
- [6] Sharma K, Deng LJ, Noguez CC. Field investigation on the performance of building structures during the April 25, 2015, Gorkha earthquake in Nepal. *Eng Struct* 2016;121:61–74.
- [7] Gong MS, Zuo ZX, Wang XM, Lu XT, Xie LL. Comparing seismic performances of pilotis and bare RC frame structures by shaking table tests. *Eng Struct* 2019;199:109442.
- [8] Guo T, Song LL, Yang K, Zhu RZ, Tesfamariam S. Experimental investigation and numerical simulation of self-centering concrete frames with sliding infill walls. *J Build Eng* 2022;52:104435.
- [9] Huang LJ, Zhou Z, Wei Y, Xie Q, Sun XY. Seismic performance and resilience assessment of friction damped self-centering prestressed concrete frames. *Eng Struct* 2022;263:114346.
- [10] Dai KS, Sun TF, Liu Y, Li T, Xu J, Bezabeh MA. Seismic performance of RC frames with self-centering precast post-tensioned connections considering the effect of infill walls. *Soil Dyn Earthq Eng* 2023;171:107969.
- [11] Stanton JF, Hawkins NM, Hicks TR. PRESSS Project 1.3-connection classification and evaluation. *PCI J* 1991;62–71.
- [12] Stone WC, Cheek GS, Stanton JF. Performance of hybrid moment-resisting precast beam-column concrete connections subjected to cyclic loading. *Acids Struct J* 1995;92(2):229–49.
- [13] Stanton J, Stone WC, GS C. A hybrid reinforced precast frame for seismic regions. *PCI J* 1997;42(2):20–32.
- [14] Cheok GS, Lew HS. Model precast concrete beam-to-column connections subject to cyclic loading. *PCI J* 1993;38(4):80–92.
- [15] Priestley MJN. Overview of PRESSS research program. *PCI J* 1991;36:50–7.
- [16] Priestley MJN, Sritharan S, Conley JR, Pampanin S. Preliminary results and conclusions from the PRESSS five-story precast concrete test building. *PCI J* 1999;44:42–67.
- [17] Priestley MJN. Direct displacement-based design of precast prestressed concrete buildings. *PCI J* 2002;47:66–79.
- [18] Englekirk RE. Design-construction of the paramount - a 39-story precast prestressed concrete apartment building. *PCI J* 2002;47(4):56–71.
- [19] Pampanin S, Kam WY, Haverland G, Gardner S. Expectation meets reality: seismic performance of post-tensioned precast concrete southern cross endoscopy building during the 22nd Feb 2011 christchurch earthquake. *NZ Concr Ind Conf* 2011.
- [20] Ozden S, Ertas O. Behavior of Unbonded, Post-Tensioned Precast Concrete Connections with Different Percentages of Mild Steel Reinforcement. *PCI J* 2007;52(2):32–44.
- [21] Wang HS, Marino EM, Pan P, Liu H, Nie X. Experimental study of a novel precast prestressed reinforced concrete beam-to-column joint. *Eng Struct* 2018;156:68–81.
- [22] Wang HS, Barbagallo F, Pan P. Test of precast pre-stressed beam-to-column joint with damage-free reinforced concrete slab. *Eng Struct* 2020;210:110368.
- [23] Wang HS, Barbagallo F, Marino EM, Pan P. Optimal design of the connection between RC slab and precast pre-stressed beam to column joint. *Eng Struct* 2022;270:114893.
- [24] Wang SG, Zhang TY, Xu WZ, Du DS, Zhang YL. Experimental and numerical investigations on novel post-tensioned precast beam-to-column energy-dissipating connections. *Structures* 2023;54:117–33.
- [25] Zhang TY, Xu WZ, Wang SG, Du DS, Xie LL, Miao QS. Seismic behavior of earthquake-damaged hybrid connections reinforced with replaceable energy-dissipating elements. *J Build Eng* 2023;80:108062.
- [26] Lu XL, Cui Y, Liu JJ, Gao WJ. Shaking table test and numerical simulation of a 1/2-scale self-centering reinforced concrete frame. *Earthq Eng Struct Dyn* 2015;44:1899–917.
- [27] Lu XL, Yang BY, Zhao B. Shake-table testing of a self-centering precast reinforced concrete frame with shear walls. *Earthq Eng Eng Vib* 2018;17:221–33.
- [28] Lu XL, Jiang C, Yang BY, Quan LM. Seismic design methodology for self-centering reinforced concrete frames. *Soil Dyn Earthq Eng* 2019;119:358–74.
- [29] Zhou Y, Song G, Huang W. Performance-based damage evaluation of hybrid joints. *B Earthq Eng* 2020;18:3781–816.
- [30] Song G, Yang TY, Zhou Y. Energy-based seismic design for self-centering concrete frames. *B Earthq Eng* 2021;19:5113–37.
- [31] Song G, Yang TY, Zhou Y. Distribution of hysteretic energy demands in self-centering concrete frames with hybrid joints. *Soil Dyn Earthq Eng* 2021;148:106828.
- [32] Song G. Performance-based damage quantification and evaluation for self-centering concrete frames. *Structures* 2023;57:105090.
- [33] Mao CX, Wang ZY. Seismic performance evaluation of a self-centering precast reinforced concrete frame structure. *Earthq Eng Eng Vib* 2021;20:943–68.
- [34] Zhu XX, Zhang ZS, Gao JH, Li WT. Two robust approaches to multicomponent signal reconstruction from STFT ridges. *Mech Syst Signal Pract* 2019;115:720–35.
- [35] Hall FE, Lombardi D, Bhattacharya S. Identification of transient vibration characteristics of pile-group models during liquefaction using wavelet transform. *Eng Struct* 2018;171:712–29.
- [36] Yuan PP, Zhang J, Feng JQ, Wang HH, Ren WX, Wang C. An improved time-frequency analysis method for structural instantaneous frequency identification based on generalized S-transform and synchroextracting transform. *Eng Struct* 2022;252:113657.
- [37] Mohebi B, Mohebi O, Kazemi F, Formisano A. Seismic damage diagnosis in adjacent steel and RC MRFs considering pounding effects through improved wavelet-based damage-sensitive feature. *J Build Eng* 2021;33:101847.
- [38] Yazdanpanah O, Mohebi B, Kazemi F, Mansouri I, Jankowski R. Development of fragility curves in adjacent steel moment-resisting frames considering pounding

- effects through improved wavelet-based refined damage-sensitive feature. *Mech Syst Signal Pr* 2022;173:109038.
- [39] Kazemi F, Asgarkhani N, Jankowski R. Machine learning-based seismic fragility and seismic vulnerability assessment of reinforced concrete structures. *Soil Dyn Earthq Eng* 2023;166:107761.
- [40] Kazemi F, Asgarkhani N, Jankowski R. Machine learning-based seismic response and performance assessment of reinforced concrete buildings. *Arch Civ Mech Eng* 2023;23:94.
- [41] Kazemi F, Asgarkhani N, Jankowski R. Predicting seismic response of SMRFs founded on different soil types using machine learning techniques. *Eng Struct* 2023;274:114953.
- [42] Kazemi F, Jankowski R. Machine learning-based prediction of seismic limit-state capacity of steel moment-resisting frames considering soil-structure interaction. *Comput Struct* 2023;274:106886.
- [43] Asgarkhani N, Kazemi F, Jankowski R. Machine learning-based prediction of residual drift and seismic risk assessment of steel moment-resisting frames considering soil-structure interaction. *Comput Struct* 2023;289:107181.
- [44] Zhang TY, Xu WZ, Wang SG, Du DS, Tang J. Seismic response prediction of a damped structure based on data-driven machine learning methods. *Eng Struct* 2024;301:117264.
- [45] Krizhevsky A., Sutskever I., Hinton G.E. ImageNet classification with deep convolutional neural networks. In: Proceedings of the twenty fifth international conference on neural information processing systems. 2012, 1097–105.
- [46] Lu XZ, Xu YJ, Tian Y, Cetiner B, Taciroglu E. A deep learning approach to rapid regional post-event seismic damage assessment using time-frequency distributions of ground motions. *Earthq Eng Struct Dyn* 2021;50:1612–27.
- [47] Su Z, Yu J, Xiao X, Wang JJ, Wang XL. Deep learning seismic damage assessment with embedded signal denoising considering three-dimensional time–frequency feature correlation. *Eng Struct* 2023;286:116148.
- [48] Ning CX, Xie YZ, Sun LJ. LSTM, WaveNet, and 2D CNN for nonlinear time history prediction of seismic responses. *Eng Struct* 2023;286:116083.
- [49] Pampinan S, Marriott D, Palermo A. PRESSS design handbook. Auckland: New Zealand Concrete Society Industry; 2010.
- [50] McKenna F, Fenves G.L. Open system for earthquake engineering simulation (OpenSees). Pacific earthquake engineering research center. University of California; 2013.
- [51] P.E.R. Center, NGA-West2 Database Flatfile, in, 2015.
- [52] GB 50011-2010. Code for seismic design of buildings. Beijing: China Construction Industry Press; 2010.
- [53] Fema B. Prestandard and commentary for the seismic rehabilitation of buildings; 2000. Washington, DC.
- [54] Thakur G, Brezdo E, Fučkar NS, Wu HT. The Synchrosqueezing algorithm for time-varying spectral analysis: robustness properties and new paleoclimate applications. *Signal Process* 2013;93:1079–94.
- [55] T/CECS 992-2022. Technical specification for application of prestressed precast concrete frame. Beijing: China Construction Industry Press; 2010.
- [56] Kunath SK, Reinhard AM, Abel JF. A computational tool for evaluation of seismic performance of reinforced concrete building. *Comput Struct* 1991;41(1):157–73.
- [57] Selvaraju R.R., Cogswell M., Das A., Ramakrishna, Vedantam, Parikh D. et al. Grad-CAM: Visual Explanations from Deep Networks via Gradient-based Localization; 2019, arXiv preprint arXiv:161002391v4.
- [58] Lundberg S.M., Lundberg S.M. A unified approach to interpreting model predictions; 2017, arXiv preprint arXiv:170507874v2.